PHYSICAL REVIEW B **109**, 134407 (2024)

Editors' Suggestion

High-order harmonics and the reverse of the squaring up process in the triangular-lattice magnet $HoPdAl_4Ge_2$

Fei Gao,[1,2] Weijun Ren,[1,2,*] Chin-Wei Wang,[3,†] S. Yano,[3] Stuart Calder,[4] Qiang Zhang,[4]
Hengheng Wu,[1,2] Meng An,[1,2] Yanpei Jing,[1,2] Bing Li,[1,2,‡] and Zhidong Zhang[1,2]
[1]Shenyang National Laboratory for Materials Science, Institute of Metal Research, Chinese Academy of Sciences, Shenyang 110016, China
[2]School of Materials Science and Engineering, University of Science and Technology of China, Shenyang 110016, China
[3]National Synchrotron Radiation Research Center, Hsinchu 300092, Taiwan
[4]Neutron Science Division, Oak Ridge National Laboratory, Oak Ridge, Tennessee 37831, USA

(Received 3 November 2023; revised 4 March 2024; accepted 5 March 2024; published 5 April 2024)

We uncover high-order harmonics and the reverse of the squaring-up process, in terms of analyzing the evolution of magnetic orders in a centrosymmetric layered triangular-lattice magnet $HoPdAl_4Ge_2$, based on a detailed study of the crystal structure, magnetic susceptibility, magnetization, heat capacity, and magnetic structure. Temperature dependencies of magnetic susceptibility and heat capacity show two magnetic transitions at $T_N = 10.5$ K and $T_t = 5.5$ K. Below T_N, Ho^{3+} spins order antiferromagnetically as a transverse spin-density wave with the propagation vector $\boldsymbol{k_1} = (0\,0\,1.5 - \delta)$ with $\delta \approx 0.18$. Upon further cooling through T_t, the high-order harmonics with $\boldsymbol{k_n} = (0\,0\,1.5 - n\delta)$, $n = 3, 5, 7$ develop, suggesting a squaring-up process. It is surprising that the squaring-up process does not continue down to 0 K but reverses the trend below 3 K. Magnetic-field-induced metastable transitions were observed in $M(H)$ curves with the fields applied both parallel and perpendicular to the triangular-lattice plane. Neutron-diffraction results suggest that the magnetization process in $HoPdAl_4Ge_2$ involves the conversion of $\boldsymbol{k_n} = (0\,0\,1.5 - n\delta)$ with $n = 1, 3, 5, 7$, to a ferromagnetic $\boldsymbol{k_F} = (0\,0\,0)$ component. It is worth noting that the already weak seventh harmonic magnetic peak is enhanced by applying a small magnetic field in the *ab* plane at 1.5 K or warming up to 3 K, accompanied by a slight decrease of δ.

DOI: 10.1103/PhysRevB.109.134407

I. INTRODUCTION

Geometric frustrated magnetic systems usually have various degenerate ground states, and the competing interactions among localized spins cannot be simultaneously satisfied. As a result, the conventional magnetic orders are suppressed. Magnetic frustration in metallic systems may induce exotic ground states, such as the quantum spin liquids and spin ice state [1–3], various spin states including spin-spiral orders, complex noncoplanar orders, and chiral magnetic structures [4,5], the electronic nematic state [6–8], the magnetic-field- and pressure-induced quantum criticality, etc. [9–16]. Magnetic frustration may also promote topologically nontrivial spin textures such as skyrmion, leading to unconventional magnetoelectric properties [17–19].

In rare-earth (R) intermetallic compounds, the complex magnetic structure may arise from geometrical frustration associated with specific lattice geometries, or from competing exchange interactions, both of which prohibit the minimization of the interaction energy acting at specific sites. The involved competing interactions are the Ruderman-Kittel-Kasuya-Yosida–type (RKKY-type) exchange coupling, while its oscillatory and long-range features often produce frustrated systems and hence cause incommensurate (helical or amplitude-modulated) magnetic structures. If a system has strong uniaxial anisotropy originating from crystalline electric field (CEF) effects, it is possible to obtain amplitude-modulated magnetic structures. Such a magnetic structure is unstable at low temperatures because the ordered magnetic moment is zero at some positions, the amplitude-modulated magnetic structure either squares up to evolve into a magnetic structure with an equal magnitude of magnetic moment in the form of appearing high-order harmonics or undergoes a lock-in magnetic transition to a commensurate magnetic structure [20,21].

The centrosymmetric layered triangular-lattice magnet $RMAl_4Ge_2$ (M = Ni, Pt, and Au) has attracted extensive research interest [22–29]. $GdAuAl_4Ge_2$ and $TbAuAl_4Ge_2$ were reported to have complex magnetic phase diagrams together with possible field-induced nontrivial spin textures [24,25], but the ground-state magnetic orders of these compounds have not been reported yet. Two successive magnetic phase transitions in zero-field and multiple field-induced magnetic states were found in the Ising-like antiferromagnet $NdAuAl_4Ge_2$ [27]. Kondo metal $CePtAl_4Ge_2$ has an incommensurate spin-density wave (SDW) order with a propagation vector $\boldsymbol{k} = (1.39\,0\,0.09)$. The magnetic excitation at 14.5 meV corresponds to the first-excited state due to the CEF splitting of the Ce^{3+} multiplet ground state [29]. To better understand the complex magnetic states of this series of materials, we choose the sister material $HoPdAl_4Ge_2$ and report the evolution of magnetic orders in this compound using neutron-diffraction techniques.

In the present work, we report crystal structure, magnetic susceptibility $\chi(T)$, magnetization $M(H)$, heat capacity

---

[*] wjren@imr.ac.cn
[†] wang.cw@nsrrc.org.tw
[‡] bingli@imr.ac.cn

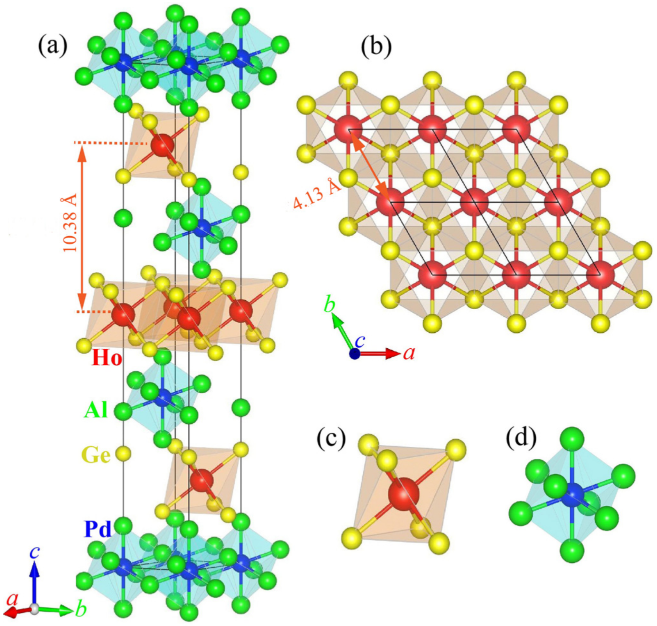

FIG. 1. (a) The schematic of $HoPdAl_4Ge_2$ crystal structure. (b) The triangular layer of magnetic distorted $HoGe_6$ octahedron in the *ab* plane. Black lines represent the unit cell. (c) The distorted $HoGe_6$ octahedron with the local point symmetry $D_{3d}(\bar{3}m)$ at the Ho site. (d) $PdAl_8$ hexahedron.

$C_P(T)$, and magnetic structure of a centrosymmetric layered triangular-lattice magnet $HoPdAl_4Ge_2$ (Fig. 1). Two anomalies at 10.5 and 5.5 K are observed in temperature-dependent magnetic susceptibility and heat capacity, and the multiple fractional magnetization states are found in $HoPdAl_4Ge_2$. The evolution of magnetic orders in metallic $HoPdAl_4Ge_2$ is studied by neutron powder diffraction (NPD) and neutron single-crystal diffraction (NSCD). The neutron-diffraction results reveal that the magnetic structure in $HoPdAl_4Ge_2$ squares up with decreasing temperature down to 3 K, and then exhibits a reversing process at lower temperatures. The evolution of magnetic orders under the applied field can explain the fractional magnetization states well.

II. EXPERIMENTAL DETAILS

Single crystals of $HoPdAl_4Ge_2$ were synthesized using the metallic flux method. High-purity starting elements 99.999% palladium powders, 99.999% aluminum cylinders and 99.999% germanium particles, and 99.5% holmium chunks were mixed with a ratio of 1 : 40 : 20 : 1, loaded into an alumina crucible, and sealed in a quartz tube under high vacuum. The mixture was slowly heated to 1323 K and held at this temperature for 10 hours to ensure that the starting materials were thoroughly melted and mixed, followed by slow cooling down to 873 K to grow crystals, and the excess flux was centrifuged at this temperature. The obtained single crystals possess typical dimensions of $\approx 2 \times 1 \times 0.5$ mm^3, as shown in the inset of Fig. 2(b). Photographs and dimensions of $HoPdAl_4Ge_2$ single crystals were measured with an optical microscope Nikon SMZ745T. The isostructural nonmagnetic $LuPdAl_4Ge_2$ single crystals were prepared by a similar method.

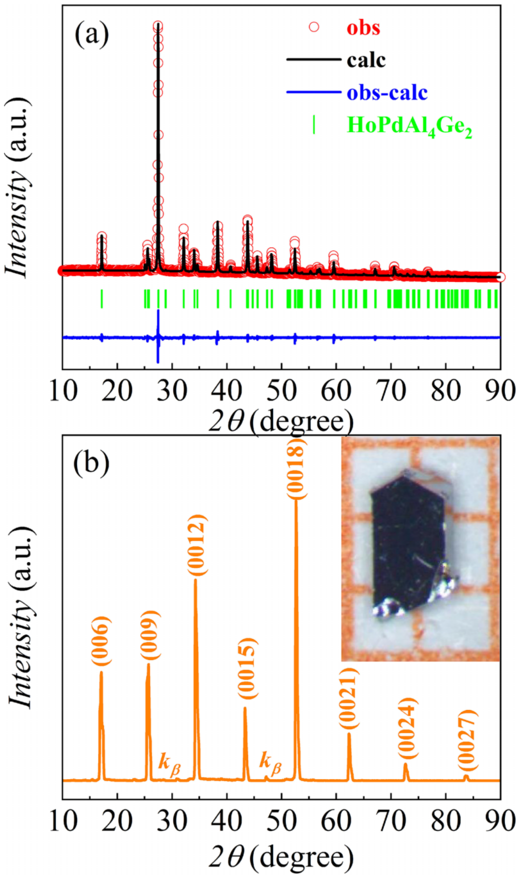

FIG. 2. (a) Powder XRD patterns and structural refinement results. (b) The XRD pattern on a flat facet of $HoPdAl_4Ge_2$ single crystal was identified as the (0 0 1) plane. The inset is a photograph of a typical $HoPdAl_4Ge_2$ single crystal on a mm-ruled grid.

The crystal structure and composition characterization were determined by a D8 Advance x-ray diffractometer with wavelength $\lambda = 1.5418$ Å and a scanning electron microscope (SEM, MERLIN Compact, ZEISS), respectively. Separate batches of polycrystalline samples prepared by grinding $HoPdAl_4Ge_2$ single crystals were sent to Oak Ridge National Laboratory (ORNL) and the Australia Nuclear Science and Technology Organization (ANSTO) for the neutron powder diffraction experiments. Temperature and magnetic-field-dependent measurements were performed on HB-2A with the wavelength of 2.41 Å at the High Flux Isotope Reactor (HFIR) at the ORNL [30,31]. On ECHIDNA (2.4395 Å) [32], the diffraction patterns were collected at 3 K to study the aging effect of the powder samples. The same sample was remeasured after being stored in ambient conditions for 21 months. The cold-neutron triple-axis spectrometer SIKA was employed for investigating the weak high-order peaks which are too weak to be seen in the powder diffraction patterns collected on HB-2A and ECHIDNA. A long neutron wavelength of 5.31 Å ($E_i = E_f = 2.9$ meV) [33,34] was chosen for the measurements with a cryocooled-cold Be-filter inserted.

A piece of $HoPdAl_4Ge_2$ single crystal was mounted at the high-intensity powder diffractometer WOMBAT of ANSTO to investigate the temperature and magnetic-field dependence of the magnetic structures [35]. WOMBAT is usually used for powder diffraction, but the two-dimensional and position-sensitive detectors make it possible to acquire reciprocal space maps from single crystals quickly. The sample was loaded in an asymmetric recondensing vertical magnet for the temperature and field-dependent measurements. A single crystal of $\approx 2 \times 2 \times 0.5$ mm^3 is mounted on a thin vanadium plate with the (H H L) plane in the scattering plane, i.e., the magnetic fields were applied along the $[1\,-1\,0]$ direction. The NSCD was measured as a function of omega angle ω (0.1° increment) to obtain the intensity mapping in the reciprocal space. The raw $\omega/2\theta$ datasets were converted into reciprocal space using the Large Array Manipulation Program (LAMP) [36]. Rietveld analysis was applied to the NPD data to obtain information on crystal and magnetic structures, employing the FullProf Suite software [37,38]. The built-in BASIREP of FullProf Suite software and the Bilbao Crystallographic Server [39,40] were utilized for identifying the magnetic space group, and the VESTA software was used to plot the crystal and magnetic structures. The magnetic susceptibility $\chi(T)$ and magnetization $M(H)$ were measured using a Magnetic Property Measurement System (XL-7, Quantum Design). Heat capacity $C_p(T)$ measurement of a HoPdAl$_4$Ge$_2$ single crystal was performed on a Quantum Design Physical Property Measurement System. A conventional thermal relaxation technique was used for heat capacity $C_p(T)$ measurements down to 2 K.

III. RESULTS AND DISCUSSION

A. Crystal structure and symmetry

HoPdAl$_4$Ge$_2$ crystallizes in the centrosymmetric $R\bar{3}m$ (No. 166) trigonal structure. As illustrated in Fig. 1(a), the crystallographically equivalent Ho ions occupy the $3b$ (0 0 0.5) Wyckoff position, located at the center of the distorted HoGe$_6$ octahedron with a local point symmetry $D_{3d}(\bar{3}m)$. The Pd ions reside in the $3a$ (0 0 0) Wyckoff position of the $\bar{3}m$ site symmetry. Ge, Al(1), and Al(2) all occupy the $6c$ $(0\,0\,z)$ of the $3m$ site symmetry, where the coordinate z is 0.22189, 0.91889, and 0.30836 for Ge, Al(1), and Al(2), respectively. The Ho^{3+} ions form a network of equilateral triangles in the ab plane and are separated by the lattice constant $a \approx 4.13$ Å. The triangular layers are stacked along the c axis in an ABC-type sequence of which the interlayer spacing is $c/3 \approx 10.38$ Å. Therefore, the interlayer interactions are expected to be weaker than the intraplane interactions. The nonmagnetic Pd and Al ions are sandwiched between these Ho triangular layers and form a PdAl$_8$ distorted hexahedron. Figure 2(a) represents the powder x-ray diffraction (XRD) pattern of HoPdAl$_4$Ge$_2$, which matches the $R\bar{3}m$ space group. The lattice constants obtained by Rietveld refinement are $a = 4.1336(1)$ Å and $c = 31.1521(4)$ Å, with the goodness-of-fit parameters $R_p = 6.732\%$, $R_{wp} = 8.848\%$, and $\chi^2 = 2.288$. The rhombohedral crystal structure persists down to 1.5 K, which is the base temperature of the NSCD experiments. The energy-dispersive x-ray (EDX) spectroscopy shows that the atomic percentages of HoPdAl$_4$Ge$_2$ are Ho, Pd, Al, Ge = 12.06, 12.08, 48.61, 27.25, close to the perfect stoichiometry 1 : 1 : 4 : 2. The XRD performed on the 2×1 mm^2 flat facet of HoPdAl$_4$Ge$_2$ single crystal is shown in Fig. 2(b) indicating that the sample has a good crystallographic orientation, and the studied facet is $(0\,0\,1)$ plane. The powder XRD patterns and Rietveld refinement plots for LuPdAl$_4$Ge$_2$ are given in Fig. S1 of the Supplemental Material [41].

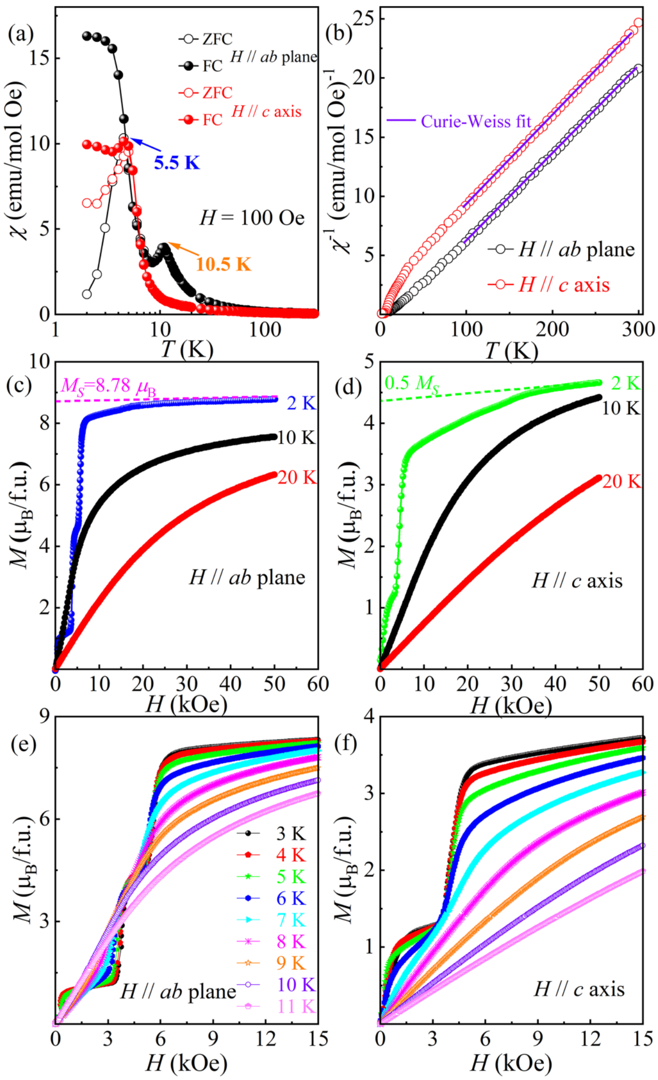

FIG. 3. (a) Temperature dependence of the ZFC and FC magnetic susceptibility. (b) The inverse magnetic susceptibility $\chi^{-1}(T)$ was measured in an applied field 1 0 0 Oe (FC mode) for both the $H \parallel ab$ plane and the $H \parallel c$ axis. The violet solid line represents a Curie-Weiss fit to the data. Field-dependent magnetization of HoPdAl$_4$Ge$_2$ for (c) the $H \parallel ab$ plane and (d) the $H \parallel c$ axis of 2, 10, and 20 K. Magnetization plotted as a function of magnetic field for the (e) $H \parallel ab$ plane and (f) $H \parallel c$ axis in the temperature range of 3–11 K.

B. Magnetic phase transition and magnetization

Figure 3(a) represents zero-field cooled (ZFC) and field-cooled (FC) magnetic susceptibility $\chi(T)$ data measured under an applied field of 1 0 0 Oe with the $H \parallel ab$ plane and the $H \parallel c$ axis. The magnetic susceptibility increases with decreasing temperature and displays a peak at around 10.5 K for the $H \parallel ab$ plane, suggesting an antiferromagnetic (AFM) transition temperature of 10.5 K. With decreasing temperature, the bifurcation of ZFC and FC curves appear below 5.5 K for both $H \parallel ab$ plane and $H \parallel c$ axis. Figure 3(b) displays the temperature dependencies of the inverse magnetic susceptibility $\chi(T)^{-1} = H/M(T)$ and the fitting by the Curie-Weiss law $\chi(T) = C/(T - \theta_{CW})$, where $C = N_A\mu_{\rm eff}^2/3k_B$ is the Curie constant, N_A is the Avogadro number, and k_B is the Boltzmann constant. The fitting of the data points above 100 K yields a positive Curie-Weiss temperature of $\theta_{CW} = 10$ K and a negative $\theta_{CW} = -22$ K for $\chi_{ab}(T)$ and $\chi_c(T)$, respectively. θ_{CW} mainly depends on the CEF effect and the magnetic interactions. In our fitting temperature range above 100 K, the CEF effect is weak, the signs of the θ_{CW} indicate the dominating FM interaction in the *ab* plane and AFM interaction along the *c* axis. The effective moments deduced from $\chi_{ab}(T)$ and $\chi_c(T)$ are 10.50 $\mu_{\rm B}$/f.u. and 10.31 $\mu_{\rm B}$/f.u., respectively. Both values agree with the calculated value of a single-ion Ho^{3+}: $\mu_{\rm eff} = g_J\sqrt{J(J+1)}\mu_B = 10.60\ \mu_{\rm B}$, with $J = 8$ and $g_J = 5/4$. Figures 3(c) and 3(d) show the field-dependent magnetization $M(H)$ pattern at 2, 10, and 20 K for the $H \parallel ab$ plane and the $H \parallel c$ axis. The magnetic-field dependence of the magnetization curves evolves with temperatures. At 2 K, multiple field-induced magnetic phase transitions appear at the low applied field (<10 kOe) for both crystallographic directions. Step-like metastable magnetic transitions with magnetization plateaus of $M/M_s \approx 0.13$ and 0.50, as shown in Fig. 4. Upon warming, the steps in magnetization curves become smooth and eventually vanish, while the critical magnetic fields decrease, as shown in Figs. 3(c)–3(f). The magnetization approaches the saturation (M_s) above ≈30 kOe for the $H \parallel ab$ plane, while the magnetization only reaches about half of the M_s for the $H \parallel c$ axis, indicating the existence of strong magnetic anisotropy. The saturation magnetization (M_s) is approximately 8.78 $\mu_{\rm B}$/f.u. at 2 K, which is significantly reduced from $g_J J = 10\ \mu_{\rm B}$, expected for a free Ho^{3+} ion.

Figures 4(a) and 4(b) demonstrate the field-dependent magnetization and the differential plot of the isotherm magnetization (dM/dH) curves up to 15 kOe at 2 K for the $H \parallel ab$ plane and for the $H \parallel c$ axis. The critical magnetic fields are demarcated by peaks in the dM/dH curve. With the magnetic field $H \parallel ab$ plane, three critical fields at $H_{c1} = 0.4$ kOe, $H_{c2} = 3.8$ kOe, and $H_{c3} = 5.6$ kOe are identified. Meanwhile, two critical fields at $H_{c1} = 0.6$ kOe and $H_{c2} = 4.4$ kOe are obtained from the $M(H)$ with the $H \parallel c$ axis. Unlike the reported $M_s/3$ magnetization plateau observed in other frustrated triangular systems [42,43], the magnetization plateaus in HoPdAl$_4$Ge$_2$ persist in a field range of several kOe with finite slopes. These features are usually found in rare-earth intermetallic compounds with a strong uniaxial anisotropy and long-range exchange interactions leading to amplitude-modulated magnetic structures [44]. From our neutron-diffraction experiments, the appearance of the multiple field-induced magnetic states in HoPdAl$_4$Ge$_2$ at 2 K originates from the response of the high-order harmonic magnetic peaks to the applied field.

C. Heat capacity

The temperature-dependent heat capacity (C_p) recorded at zero magnetic field is shown in Fig. 5 for HoPdAl$_4$Ge$_2$ and nonmagnetic isostructural compound LuPdAl$_4$Ge$_2$. In HoPdAl$_4$Ge$_2$, the C_p decreases with decreasing temperature and exhibits two anomalies, a λ-shaped peak at 10.5 K and a dim slope change at 5.5 K, in agreement with the observation of magnetic phase transitions in the $M(T)$ data. As illustrated in Fig. 5(b), the data of $C_p(T)$ above 15 K is fitted using the Debye-Einstein model to estimate the electronic (C_{el}) and phononic (C_{ph}) contributions to heat capacity:

$$C_{el+ph}(T) = \gamma T + \alpha 9NR\left(\frac{T}{\theta_D}\right)^3 \int_0^{\theta_D/T} \frac{x^4 e^x}{(e^x - 1)^2}dx + (1-\alpha)3NR\frac{(\Theta_E/T)^2 e^{\theta_E/T}}{(e^{\theta_E/T} - 1)^2},$$

where θ_D and θ_E are the Debye and Einstein temperatures, respectively. The coefficients α and $1-\alpha$ denote the contribution of Debye and Einstein terms to the phonon heat capacity, respectively. The fit yields $\theta_D = 156$ K, $\theta_E = 357$ K, $\alpha =$

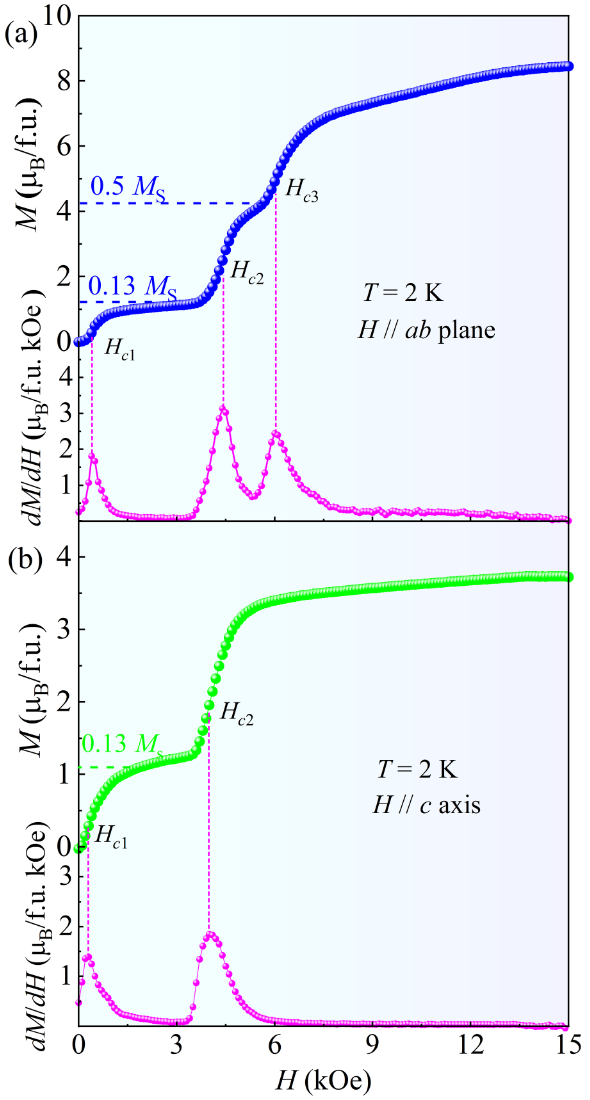

FIG. 4. Isothermal magnetization and field-dependent dM/dH curve measured at 2 K with the applied field along (a) the *ab* plane and (b) the *c* axis. The vertical pink dashed lines indicate the critical fields.

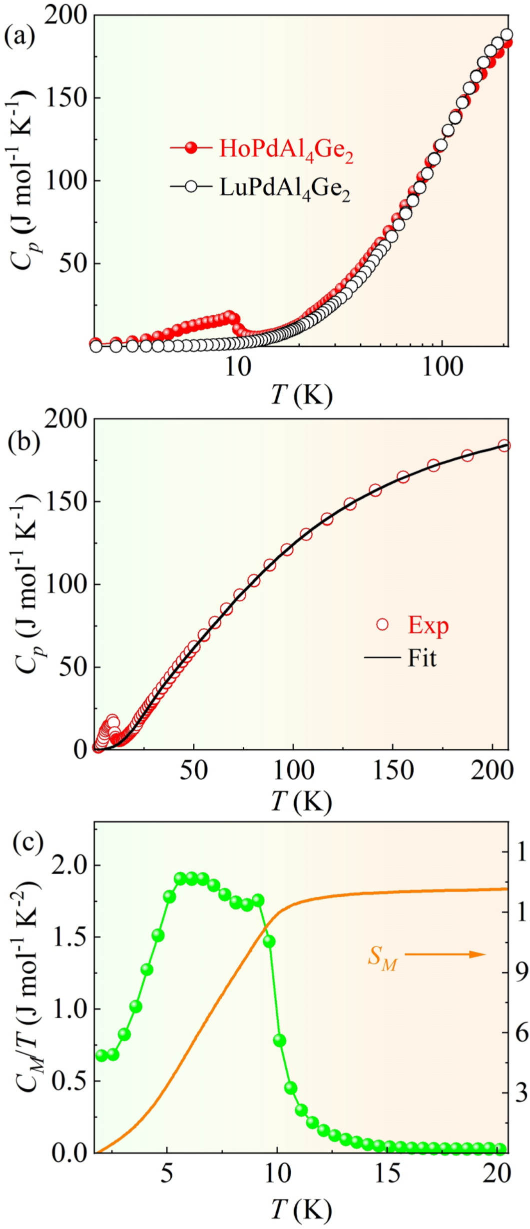

FIG. 5. (a) Temperature-dependent heat capacity of HoPdAl$_4$Ge$_2$ (red circles, C_{Ho}) and nonmagnetic LuPdAl$_4$Ge$_2$ (black circles, C_{Lu}) in zero fields. (b) Temperature dependence of heat capacity for HoPdAl$_4$Ge$_2$. The black line represents the fit using the Debye-Einstein model. (c) Temperature dependence of the magnetic heat capacity with the nonmagnetic contributions removed (left ordinate). Temperature dependence of magnetic entropy S_M of HoPdAl$_4$Ge$_2$ (right ordinate).

0.42, and the electronic specific-heat coefficient $\gamma = 0.056$ J mol^{-1} K^{-2}. The magnetic heat capacity C_M of HoPdAl$_4$Ge$_2$ with the nonmagnetic contributions subtracted is shown in Fig. 5(c). A broad hump is observed between 5.5 and 10.5 K, indicating the possible influence of magnetic frustration between the Ho^{3+} moments. The absence of a sharp ordering feature in the heat capacity is a typical signature of frustrated magnetic materials, where the magnetic moments cannot order onto a unique, lowest energy state [5]. We calculate the magnetic entropy (S_M) of HoPdAl$_4$Ge$_2$ by using the formula $S_M = \int_0^T [C_M(T)/T]dT$. The integrated S_M of HoPdAl$_4$Ge$_2$ increases with increasing temperature and reaches a saturation value of 13.2 J mol^{-1} K^{-1} at 10.5 K [seen in the right ordinate in Fig. 5(c)], far below the theoretical value of 23.6 J mol^{-1} K^{-1} calculated from $S_M = R\ln(2J+1)$ with $J = 8$. They are only 18.1% and 55.9% of the full magnetic entropy (23.6 J mol^{-1} K^{-1}) at 5.5 and 10.5 K, respectively, implying a large influence of the CEF effect on the Ho^{3+} ions [45–47].

D. Evolution of magnetic orders: Temperature dependence

The magnetic structures of HoPdAl$_4$Ge$_2$ are studied employing powder and single-crystal neutron diffraction. A wide-two-theta-range diffraction intensity map was collected at the base temperature (see Supplemental Material Fig. S6). It is seen that the magnetic peaks line up with $(0\,0\,L)$ and $(1\,1\,L)$, indicating that the magnetic modulation is along the c axis. The temperature-dependent measurements were conducted in a reduced range around the $(0\,0\,6)$ peak, as shown in Fig. 6. At 9 K, two pairs of magnetic peaks appear on the two sides of $(0\,0\,6)$, and these peaks can be indexed as $(0\,0 \approx 4.32)$, $(0\,0 \approx 4.68)$, $(0\,0\,7.32)$, and $(0\,0 \approx 7.68)$. The magnetic structure is characterized by an incommensurate wave vector $\boldsymbol{k_1} = (0\,0\,1.5 - \delta)$, where the incommensurability, $\delta \approx 0.18$. Upon cooling, additional peaks appear on both wings of the pairs of high-temperature peaks, and accordingly, these additional peaks can be indexed with $\boldsymbol{k_n} = (0\,0\,1.5 - n\delta)$. The additional peaks with $n = 3$ at 7 and 5 K, while those with $n = 5$ and 7 show up at 3 K. The value of δ is essentially constant in temperature above 3 K but is getting slightly larger at 1.5 K. The high-order harmonics are also observed in powder data. The $n = 1$ and 3 are visible in the NPD data collected on HB-2A (Fig. 7) and ECHIDNA [see Supplemental Material Fig. S7(a)], while $n = 5$ harmonics can barely be identified in the data collected with the triple-axis spectrometer, SIKA (see Supplemental Material Fig. S8). Notably, the commensurate $(0\,0\,1.5)$ phase does not appear in the single-crystal diffraction data, while incorporating such a phase could improve the fitting quality for the powder data. The emergence of odd-order harmonics generally refers to the squaring-up of an amplitude-modulated incommensurate spin structure [48–52]. Therefore, the amplitude-modulated spin structure, i.e., the spin-density wave (SDW) model, was employed in the Rietveld analysis of the NPD data. Given that the $(0\,0\,L) \pm \boldsymbol{k}$ magnetic peaks are most intense, and the easy-plane anisotropy features present in the magnetometry data, the spins are most likely lying in the ab plane. In the analysis of NPD data, up to three magnetic phases are added to account for different propagation vectors, and all the scale factors are constrained to be identical to the nuclear structure phase. Rather than considering the coexistence of multiple magnetic structures in the sample, treating the overall magnetic structure as a Fourier sum of sine waves with different wave vectors is more suitable. Each magnetic phase other than $\boldsymbol{k_0} = (0\,0\,1.5)$ describes a sine wave with a wave vector, and the magnetic moment in each phase is the mode amplitude for the wave vector. The magnetic structure for each magnetic phase is illustrated in Fig. 8. The magnetic structure with the commensurate wave vector $\boldsymbol{k_0} = (0\,0\,1.5)$ is a collinear antiferromagnet. Ferromagnetic triangular-lattice layers are stacking alternatively along the c axis, as shown

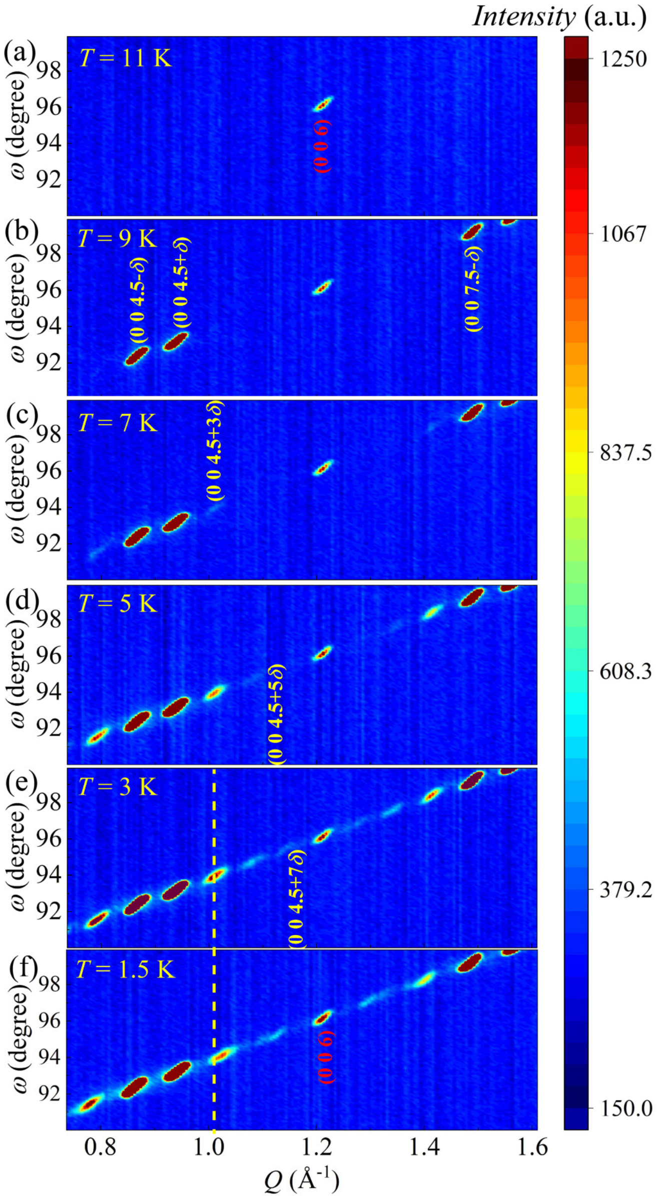

FIG. 6. Contour plots of the zero-field elastic neutron-scattering pattern around the (0 0 6) plane taken at Wombat at (a) 11 K, (b) 9 K, (c) 7 K, (d) 5 K, (e) 3 K, and (f) 1.5 K. The indexes of the strongest nuclear and magnetic reflections of each propagation vector are provided. The vertical yellow dashed line is used to emphasize the change in δ.

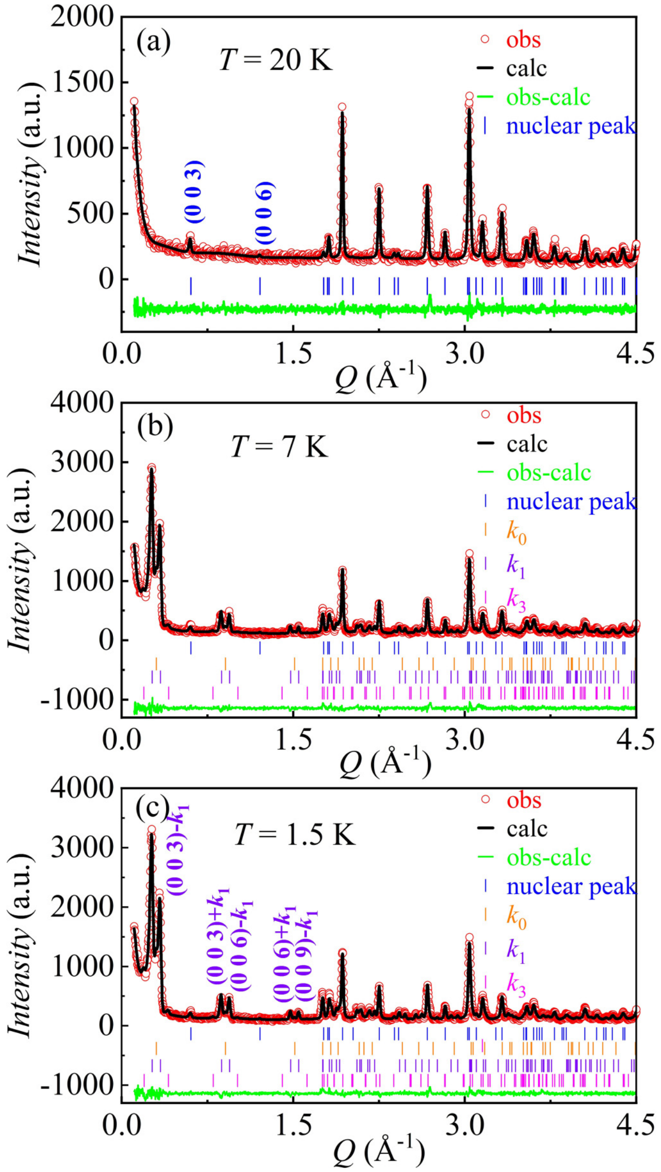

FIG. 7. Rietveld refinement results of the NPD patterns on HB-2A for HoPdAl$_4$Ge$_2$ at (a) 20 K, (b) 7 K, and (c) 1.5 K with neutron wavelength $\lambda = 2.41$ Å. The orange, violet, and pink vertical lines in this case indicate the magnetic reflections $\boldsymbol{k_0} = (0\,0\,1.5)$ and the first and third harmonics, respectively, while the blue (top) vertical lines indicate the nuclear structure.

in Fig. 8(a). The $\boldsymbol{k_n} = (0\,0\,1.5 - n\delta)$ phases are all transverse spin-density waves with the magnitude of the spin modulated along the c axis [Fig. 8(b)]. The refined incommensurability $\delta = 0.1754(2)$ at 7 K is slightly smaller than $\delta = 0.1764(2)$ at 1.5 K. That is consistent with the single-crystal diffraction results. The magnetic moments obtained from the Rietveld refinement read 2.186(31) μ_B [2.285(31) μ_B], 8.568(34) μ_B [9.098(39) μ_B], and 1.851(59) μ_B [2.006(56) μ_B] for the wave vector $\boldsymbol{k_n} = (0\,0\,1.5 - n\delta)$ with $n = 0$, 1, and 3, respectively at 7 K (1.5 K). The amplitude ratio between the third and first harmonics, $\mu_{n=3}/\mu_{n=1}$ is 1/3 for a perfect square wave, while the ratio of $\mu_{n=3}/\mu_{n=1}$ is about 0.216 and 0.221 for HoPdAl$_4$Ge$_2$ at 7 and 1.5 K, respectively. The temperature dependence of the $\mu_{n=3}/\mu_{n=1}$ ratio suggests that the spin structure would not totally square up. Furthermore, as shown in Fig. 6(f), the seventh harmonic vanishes at 1.5 K instead of strengthening. The square-up process is retarding at low temperatures.

E. Evolution of magnetic orders: Magnetic-field dependence

Magnetic-field-dependent single-crystal diffraction was conducted on WOMBAT with a vertical cryomagnet. The crystal was aligned to the $(H\,H\,L)$ scattering plane and the magnetic fields were applied perpendicular to the scattering plane, i.e., along the $[1\,{-1}\,0]$ direction. The diffraction intensities map $I(Q, \omega)$ around the $(0\,0\,6)$ reflection collected

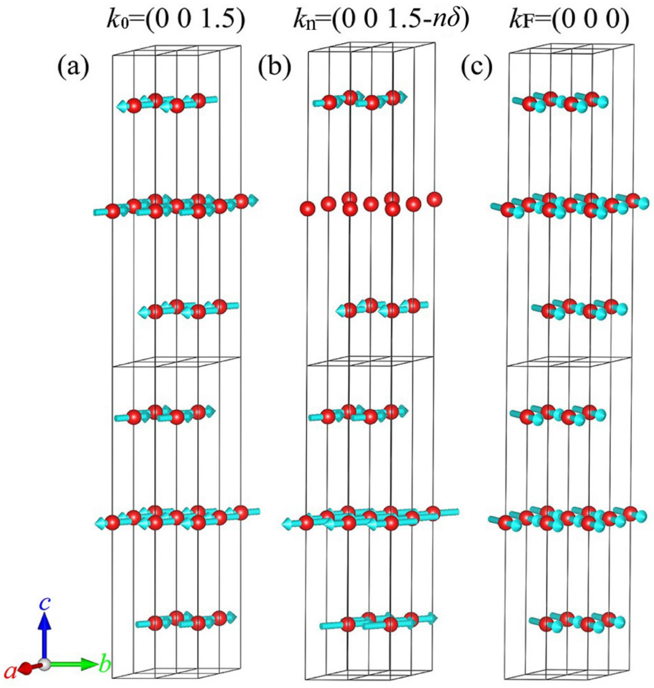

FIG. 8. Zero-field magnetic structures at 1.5 K of (a) commensurate $\boldsymbol{k_0} = (0\,0\,1.5)$ and (b) incommensurate $\boldsymbol{k_n} = (0\,0\,1.5 - n\delta)$. (c) Field-induced ferromagnetic structure of $\boldsymbol{k_F} = (0\,0\,0)$ with the magnetic moments lying in the *ab* plane. Atoms other than Ho have been removed for clarity.

at 1.5 K, under some selected magnetic-field strengths, are illustrated in Fig. 9. From $H = 0$ to 2.5 kOe, the seventh harmonic surprisingly appears, and the incommensurability, δ slightly decreases. Afterward, the incommensurate peaks are suppressed, and the commensurate $(0\,0\,6)$ is enhanced upon increasing the magnetic-field strength. The field dependence of the incommensurate peaks upon field increasing mimics what happens during warming. The fifth and seventh harmonics vanish at magnetic fields slightly higher than 5 and 7.5 kOe, respectively. The first-order incommensurate peaks vanish between 10 and 20 kOe. When the incommensurate peaks at $(h\,k\,l) \pm \boldsymbol{k_n}$ are suppressed, their intensities are redistributed to the commensurate peak positions, such as $(0\,0\,6)$. The field-induced commensurate magnetic structure is illustrated in the field-dependent NPD results as a ferromagnetic structure with the moments pointing to the external field direction $[1\,-1\,0]$ [Fig. 8(c)].

The sample for NPD is a pressed pellet of ground $\mathrm{HoPdAl_4Ge_2}$ single crystals; it is expected that the metamagnetic transitions would last for a wider field range in the powder samples due to the distribution of the local field direction for each grain. The field-dependent NPDs are still useful for understanding the magnetization process. Figure 10 collects the NPD data measured at 1.5 K under the magnetic-field strengths up to 50 kOe. Despite the high-order harmonics with $n \geqslant 5$ being too weak to be identified in powder patterns and the absence of $\boldsymbol{k_0} = (0\,0\,1.5)$ in the single-crystal data, consistent results are observed, where the

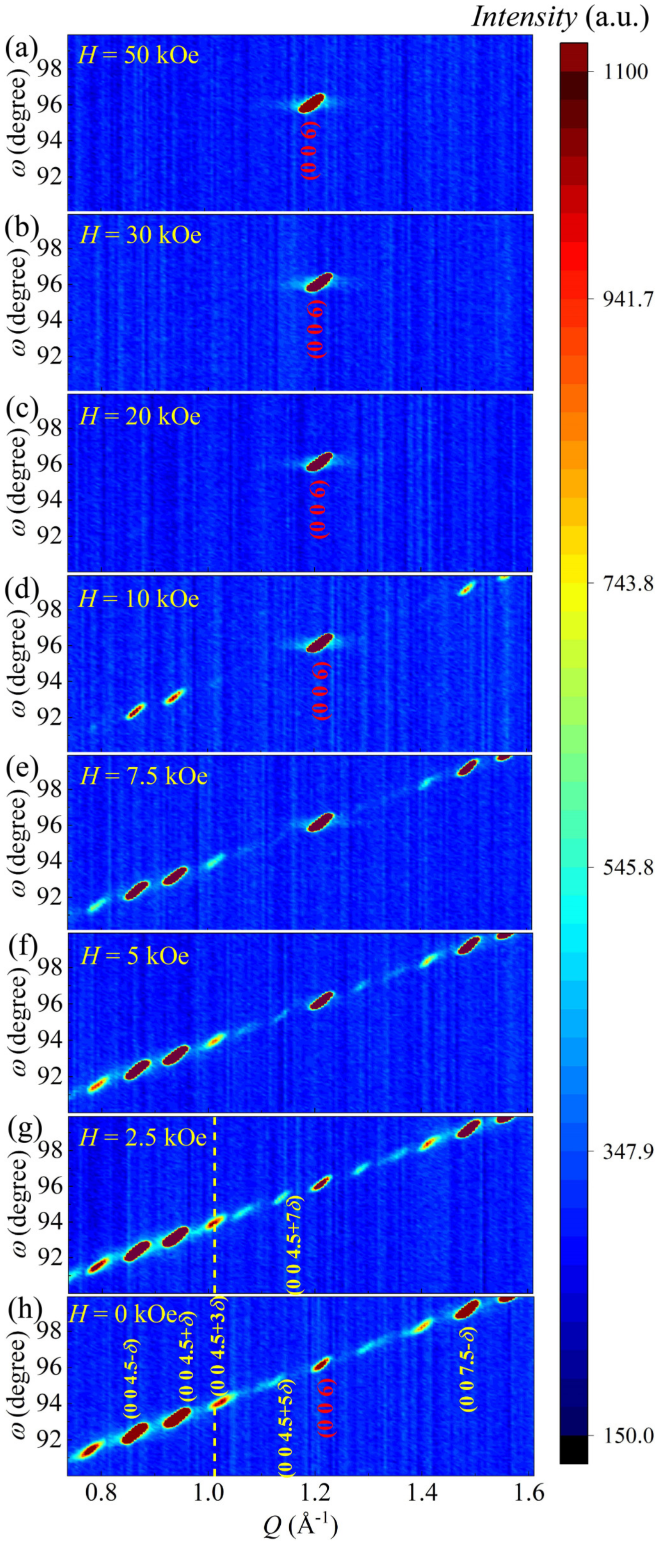

FIG. 9. Neutron single-crystal diffraction collected under some selected magnetic-field strengths: (a) 50 kOe, (b) 30 kOe, (c) 20 kOe, (d) 10 kOe, (e) 7.5 kOe, (f) 5 kOe, (g) 2.5 kOe, and (h) 0 kOe at 1.5 K. The crystal is aligned with the $(H\,H\,L)$ plane in the scattering plane, and the magnetic field is applied along the $[1\,-1\,0]$ direction. The vertical yellow dashed line is used to emphasize the change in δ.

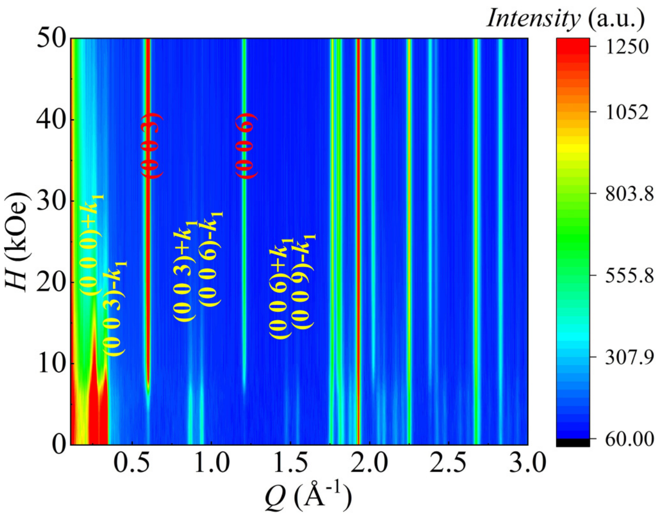

FIG. 10. Field evolution of overall neutron scattering for $HoPdAl_4Ge_2$ powder at 1.5 K. The indexes of the strongest nuclear or magnetic reflections of each propagation vector are provided.

incommensurate $\boldsymbol{k_n} = (0\,0\,1.5 - n\delta)$ peaks are suppressed and are redistributed to the zero wave vector positions. In addition to the $\boldsymbol{k_n} = (0\,0\,1.5 - n\delta)$ phases, the $\boldsymbol{k_F} = (0\,0\,0)$ phase is appended as a separate magnetic phase to fit the NPD patterns collected under the magnetic fields. Due to the strong (0 0 3) and (0 0 6) peaks, the magnetic moments in the field-induced $\boldsymbol{k_F} = (0\,0\,0)$ phase are expected to be in the *ab* plane. The Rietveld plots of the field-dependent NPD are shown in Fig. 11. The obtained magnetic moment for each phase is plotted in Fig. 12(a) as a function of the magnetic field, and the structural parameters are summarized in Table S2 of the Supplemental Material [41]. Overall, all antiferromagnetic components $\boldsymbol{k_n} = (0\,0\,1.5 - n\delta)$ with $n = 0$, 1, and 3 are converted to the ferromagnetic component $\boldsymbol{k_F} = (0\,0\,0)$ by the magnetic field. In the low-field regime, the third harmonic is reduced quicker than that of the first harmonic. Meanwhile, the ratio $\mu_{\rm n=3}/\mu_{\rm n=1}$ decreases from $\approx$0.22 at zero field to $\approx$0.13 at 6 kOe, manifesting a revering process of the squaring-up. The $n = 3$ harmonic becomes too weak to be identified in the NPD above $H = 6$ kOe but is still visible up to 10 kOe in single-crystal results. The NPD patterns collected between 8 and 30 kOe were analyzed with a spin-density wave and a ferromagnetic phase. In the 50 kOe pattern, the antiferromagnetic components, $\boldsymbol{k_n} = (0\,0\,1.5 - n\delta)$ with $n = 0$, 1, and 3, have all been converted to the $\boldsymbol{k_F} = (0\,0\,0)$ phase, giving a ferromagnetic moment of 7.792(54) $\mu_{\rm B}$ per Ho^{3+}. The refined magnetic structures for all the wave vectors have noticeably reduced moments compared with the 10 $\mu_{\rm B}$ expected for a free Ho^{3+}, this could be from the incomplete saturation of the Ho moment from applied field.

The powder samples were obtained by fully grinding single crystals. The anisotropic response is neglected in the NPD data analysis, and the spin arrangement in each grain is assumed to be identical. Despite that the compound is magnetically anisotropic (Figs. 3 and 4) and the external magnetic field exerts different influence on the grain with different related orientations to the applied field. In general, the values obtained by NPD in magnetic fields do not reflect the actual magnetic moments. However, in the current rhombohedral case (in hexagonal setting) with in-plane magnetic anisotropy, the actual spin canting away from the coplanar models would be quite small. In addition, the spin orientations within the hexagonal plane are not resolvable by NPD. Therefore, we recommend that our analysis of the field-dependent NPD is a good approximation of the reality. As shown in Fig. 12(b), we also extracted the peak intensities of $\boldsymbol{k_F}$, $\boldsymbol{k_1}$, $\boldsymbol{k_3}$, and $\boldsymbol{k_5}$ from the NSCD data at 1.5 K, even can be seen in Figs. 6 and 9, whereas the $\boldsymbol{k_5}$ component is too weak to be reliably extracted. In the temperature and magnetic-field dependencies of the NSCD, the data were collected in a limited omega range. Due to the lack of enough magnetic Bragg peaks, the magnetic moments cannot be deduced accurately. But the field dependencies of these peaks show a very similar trend to what is observed in the NPD data as shown in Fig. 12(a).

IV. DISCUSSION

The RKKY interaction between the localized 4*f* moments is the dominant magnetic coupling in the heavy rare-earth intermetallic compounds. The long-range interactions mediated by the conduction electrons could enhance the probability of frustration in the metallic compounds by considering the far-distanced ion pairs. The magnetometry measurements reveal that the major magnetic interaction in the *ab* plane of $HoPdAl_4Ge_2$ is ferromagnetic, excluding the geometric magnetic frustration on the triangular-lattice. The mild frustration parameter, $f = |\theta_{CW}/T_N| < 2.1$, along the *c* axis, indicates that a weak magnetic frustration could occur between the nearest and next-nearest neighboring planes, which results in the incommensurate magnetic ordering propagating along the *c* axis. The Ho^{3+} spins undergo the long-range magnetic phase transition at $T_N = 10.5$ K, into a magnitude-modulated spin structure with the wave vector, $\boldsymbol{k_1} = (0\,0\,1.5 - \delta)$, where δ is about 0.1789. When the temperature further decreases, the modulated structure becomes energetically unfavored and would transform into the equal moments structures, such as commensurate AFM, antiphase domain structure, or square wave structure [48–51]. The appearance of the odd-order harmonics in the neutron-diffraction results supports such a squaring-up process that takes place in the title compound. It can be understood that the squaring-up process helps to reduce the free energy of the system. However, the magnitude-modulated magnetic structure is not totally squaring-up down to the base temperature of this work and very likely would not transform to an equal moment structure by following the high-temperature trend of $\mu_{\rm n=3}/\mu_{\rm n=1}$. This is consistent with the fact that Ho^{3+} is not a Kramers ion, so the modulated structure could remain stable down to 0 K [52]. Actually, the reverse process of the squaring-up is observed at low temperatures, where high-order harmonics are getting weaker, and the seventh harmonic disappears upon cooling from 3 to 1.5 K.

Metamagnetic phase transitions occur when an antiferromagnet phase has a strong enough magnetic field applied to overcome the antiferromagnetic exchange couplings or the magnetic anisotropy, resulting in jumps or plateaus in the magnetization curves. The magnetization plateaus could result from various mechanisms but must involve the development

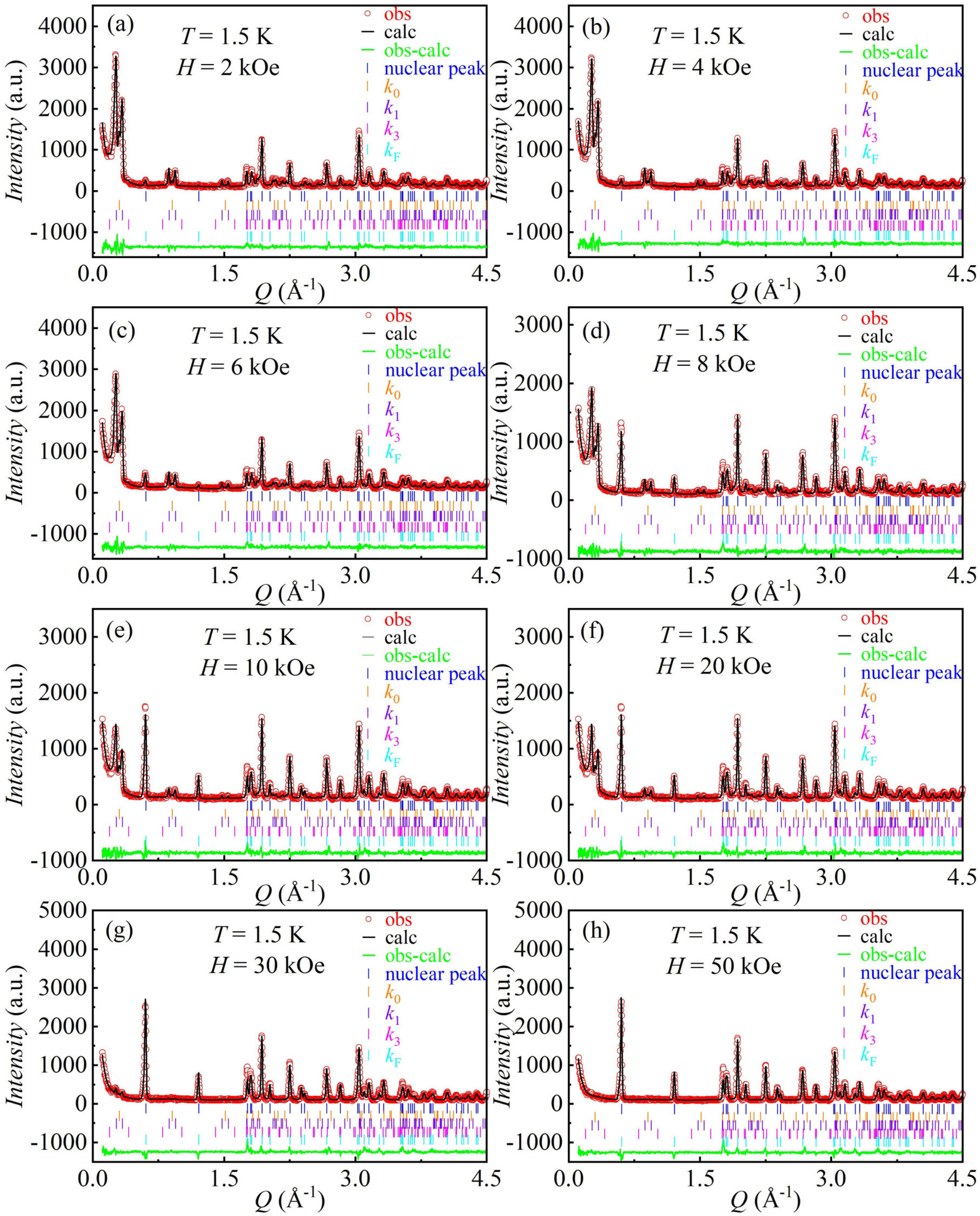

FIG. 11. Rietveld refinement plots of the NPD pattern measured under (a) 2 kOe, (b) 4 kOe, (c) 6 kOe, (d) 8 kOe, (e) 10 kOe, (f) 20 kOe, (g) 30 kOe, (h) 50 kOe of HB-2A at 1.5 K.

of uncompensated moments in the magnetic structure, such as the up-up-down 1/3-plateau in geometrically frustrated spin-1/2 triangular-lattice [42,43], pulse-wave structure [53], quantized magnetization plateau [54], etc. Our magnetic-field-dependent neutron-diffraction experiments indicate that the magnetization process in $\mathrm{HoPdAl_4Ge_2}$ is correlated with the conversion of antiferromagnetic $\boldsymbol{k_n} = (0\,0\,1.5 - n\delta)$ components to the ferromagnetic component $\boldsymbol{k_F} = (0\,0\,0)$ phase. The antiferromagnetic components are extinct when the applied field strength is above 10 kOe in the single crystal, and 30 kOe in the powder data. The $\boldsymbol{k_n}$ and $\boldsymbol{k_F}$ should be considered as the Fourier components of a single magnetic structure. The overall magnetic structure could be a pulse-train structure with a different number of up spins and down spins or a "two-dimensional (2D) analog of the three-dimensional (3D) conical" spin structure (fan structure) when the coplanar $\boldsymbol{k_n}$ and $\boldsymbol{k_F}$ magnetic moments are collinear or orthogonal, as shown in Figs. 13(b) or 13(c).

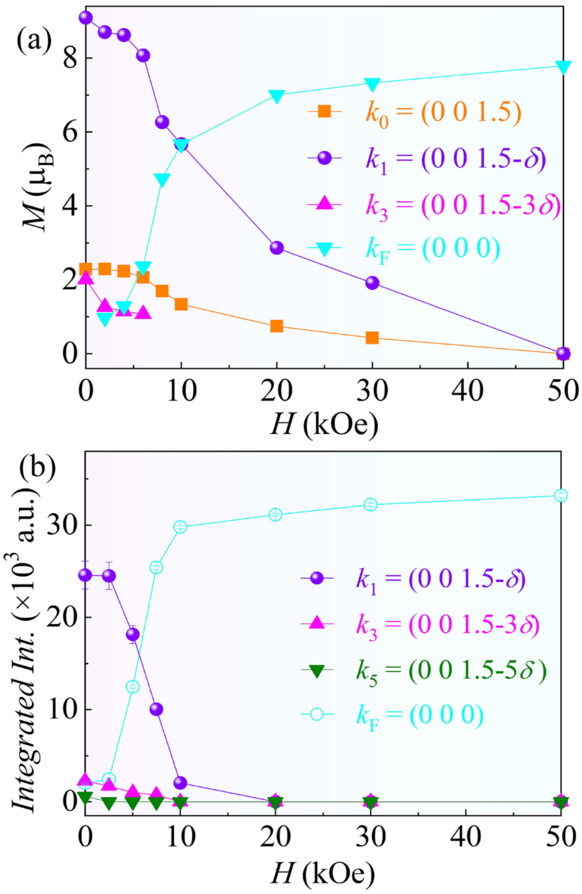

FIG. 12. (a) Field-dependent Ho^{3+} ion magnetic moment for different $\boldsymbol{k}$ vectors obtained by NPD at 1.5 K. (b) Field-dependent integrated neutron-diffraction intensity for different $\boldsymbol{k}$ vectors obtained by NSCD at 1.5 K.

The seventh harmonic is enhanced by applying a small magnetic field in the *ab* plane at 1.5 K before the induced ferromagnetic state is reached, due to the increasing field lowers the free energy of the incommensurate phase more rapidly than that of the simple ones [44,55].The recovery of high-temperature propagation vectors during low-temperature magnetization process was also observed in other compounds with amplitude-modulated magnetic structures, such as $PrCo_2Si_2$ [56], $TbNi_2Si_2$ [57], and HoAlGa [58]. Note that all these phenomena arise from exchange interactions alone, while the role of CEF acting only to impose the direction of magnetic moment and fix the magnetism of the ground state.

(a) Square wave, $\boldsymbol{k_n}$ // c, $m(\boldsymbol{k_n})$ // a

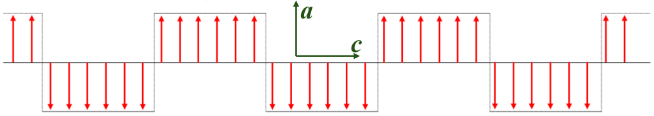

(b) $m(\boldsymbol{k_F})$ // $m(\boldsymbol{k_n})$ // a

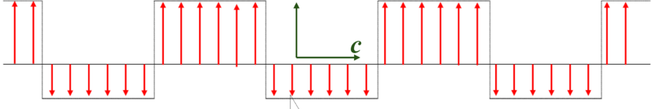

(c) $m(\boldsymbol{k_F}) \perp m(\boldsymbol{k_n})$

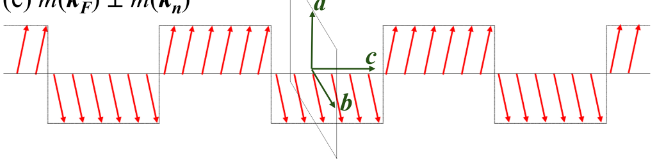

FIG. 13. The schematic diagram of (a) a perfect square wave, (b) a pulse-train structure, and (c) a two-dimensional fan structure.

The commensurate wave vector $\boldsymbol{k_0} = (0\,0\,1.5)$ is the biggest discrepancy between powder and single-crystal neutron-diffraction results. In this investigation, all the powder samples for NPD are obtained by grinding single crystals. This grinding process might have caused the distinction between the samples, such as slightly inhomogeneous composition. A similar situation has been reported in $NpPd_2Al_3$, the coexistence of two magnetic phases in polycrystalline samples may arise from slightly different stoichiometry or lattice distortions [59]. The magnetic ordering in the heavy rare-earth compounds is dominated by the structure of the Fermi surface. The magnetic order would adopt a periodicity $\boldsymbol{q_0}$, which is the maximum in the Fourier transform of the RKKY exchange interaction $J(\boldsymbol{q})$. We are currently unable to give a real reason for the discrepancy. We reinvestigated the same sample on ECHIDNA after storing them in ambient conditions for 21 months, as shown in Fig. S7(b) of the Supplemental Material [41], the refinement of the diffraction pattern gives magnetic moments from the old and new data are essentially identical.

V. CONCLUSION

To summarize, we have systematically studied the evolution of magnetic order and physical properties of the centrosymmetric metallic $HoPdAl_4Ge_2$ single crystal. $HoPdAl_4Ge_2$ crystallizes in the $R\bar{3}m$ space group with Ho^{3+} ion in triangular-lattice layers. Two anomalies at 10.5 K (T_N) and 5.5 K (T_t) are found both in temperature dependence of magnetic susceptibility and heat capacity. The magnetic entropy reaches a saturation value of 13.2 J mol^{-1} K^{-1} at 10.5 K far below the theoretical value, indicating a large effect from the CEF. The magnetometry and neutron-diffraction experiments show that $HoPdAl_4Ge_2$ is a nongeometric frustrated, incommensurate antiferromagnet with an easy-plane anisotropy. With decreasing temperature, the high-order harmonics and the reverse of the squaring-up process were found in this compound. A sinusoidally modulated spin structure develops below T_N, while the high-order satellite peaks, indexed by wave vector $\boldsymbol{k_n} = (0\,0\,1.5 - n\delta)$ where n is an odd integer, emerge below T_t, manifesting the squaring-up process commonly observed in the localized $4f$ or $5f$ compounds with an incommensurate spin structure, but the squaring-up process does not continue down to 0 K and reverses the trend below ≈3 K. Upon applying magnetic fields, the antiferromagnetic $\boldsymbol{k_n} = (0\,0\,1.5 - n\delta)$ components are converted to the ferromagnetic $\boldsymbol{k_F} = (0\,0\,0)$ component and the steps in $M(H)$ are associated with the response of $\boldsymbol{k_n}$ to the magnetic field. A recovery of the high-order harmonic was observed during the low-temperature magnetization process. Further inelastic neutron-scattering experiments at zero field and high magnetic fields are required to unveil the exchange interactions for a deep understanding of the appearance of the high-order harmonics and the reverse of the squaring-up process in $HoPdAl_4Ge_2$.

ACKNOWLEDGMENTS

This work was supported by the Ministry of Science and Technology of China (Grants No. 2020YFA0406002 and No. 2021YFB3501201) and the National Natural Science Foundation of China (Grant No. 52071323). We acknowledge the high-intensity powder diffractometer WOMBAT, high-resolution powder diffractometer ECHIDNA, and multiplexing cold-neutron triple-axis spectrometer SIKA of the ANSTO for neutron beam time. This research used resources at the High Flux Isotope Reactor, a DOE Office of Science User Facility operated by the Oak Ridge National Laboratory.

---

[1] L. Balents, Spin liquids in frustrated magnets, Nature (London) **464**, 199 (2010).

[2] H. T. Diep, *Frustrated Spin Systems* (World Scientific, Beijing, 2004).

[3] M. J. Harris, S. T. Bramwell, D. F. McMorrow, T. Zeiske, and K. W. Godfrey, Geometrical frustration in the ferromagnetic pyrochlore $Ho_2Ti_2O_7$, Phys. Rev. Lett. **79**, 2554 (1997).

[4] K. Zhao, H. Deng, H. Chen, K. A. Ross, V. Petříček,G. Günther, M. Russina, V. Hutanu, and P. Gegenwart, Realization of the kagome spin ice state in a frustrated intermetallic compound, Science **367**, 1218 (2020).

[5] C. Lacroix, P. Mendels, and F. Mila, *Introduction to Frustrated Magnetism*, in Springer Series in Solid State Sciences (Springer, 2011), Vol. 164.

[6] F. Ronning, T. Helm, K. R. shirer, M. D. Bachmann, L. Balicas, M. K. Chan, B. J. Ramshaw, R. D. McDonald, F. F. Balakirev, M. Jaime, E. D. Bauer, and P. J. W. Moll, Electronic in-plane symmetry breaking at field-tuned quantum criticality in $CeRhIn_5$, Nature (London) **548**, 313 (2017).

[7] D. M. Fobes, S. Zhang, S.-Z. Lin, Pinaki Das, N. J. Ghimire, E. D. Bauer, J. D. Thompson, L. W. Harriger, G. Ehlers, A. Podlesnyak, R. I. Bewley, A. Sazonov, V. Hutanu, F. Ronning, C. D. Batista, and M. Janoschek, Tunable emergent heterostructures in a protypical correlated metal, Nat. Phys. **14**, 456 (2018).

[8] P. F. S. Rosa, S. M. Thomas, F. F. Balakirev, E. D. Bauer, R. M. Fernandes, J. D. Thompson, F. Ronning, and M. Jaime, Enhanced hybridization sets the stage for electronic nematicity in $CeRhIn_5$, Phys. Rev. Lett. **122**, 016402 (2019).

[9] K. Mochidzuki, Y. Shimizu, A. Kondo, S. Nakamura, S. Kittaka, Y. Kono, T. Sakakibara, Y. Ikeda, Y. Isikawa, and K. Kindo, Thermodynamic investigation of metamagnetic transitions and partial disorder in the quasi-kagome Kondo lattice CePdAl, J. Phys. Soc. Jpn. **86**, 034709 (2017).

[10] H. Zhao, J. Zhang, M. Lyu, S. Bachus, Y. Tokiwa, P. Gegenwart, S. Zhang, J. Cheng, Y.-f. Yang, G. Chen, Y. Isikawa, Q. Si, F. Steglich, and P. Sun, Quantum-critical phase from frustrated magnetism in a strongly correlated metal, Nat. Phys. **15**, 1261 (2019).

[11] V. Fritsch, N. Bagrets, G. Goll, W. Kittler, M. J. Wolf, K. Grube, C. L. Huang, and H. v. Löhneysen, Approaching quantum criticality in a partially geometrically frustrated heavy-fermion metal, Phys. Rev. B **89**, 054416 (2014).

[12] J. Zhang, H. Zhao, M. Lv, S. Hu, Y. Isikawa, Y. F. Yang, Q. Si, F. Steglich, and P. Sun, Kondo destruction in a quantum paramagnet with magnetic frustration, Phys. Rev. B **97**, 235117 (2018).

[13] Y. Tokiwa, M. Garst, P. Gegenwart, S. L. Bud'ko, and P. C. Canfield, Quantum bicriticality in the heavy-fermion metamagnet YbAgGe, Phys. Rev. Lett. **111**, 116401 (2013).

[14] Y. Tokiwa, C. Stingl, M.-S. Kim, T. Takabatake, and P. Gegenwart, Characteristic signatures of quantum criticality driven by geometrical frustration, Sci. Adv. **1**, e1500001 (2015).

[15] R. Küchler, C. Stingl, Y. Tokiwa, M. S. Kim, T. Takabatake, and P. Gegenwart, Uniaxial stress tuning of geometrical frustration in a Kondo lattice, Phys. Rev. B **96**, 241110(R) (2017).

[16] C. L. Yang, S. Tsuda, K. Umeo, Y. Y amane, T. Onimaru, T. Takabatake, N. Kikugawa, T. Terashima, and S. Uji, Quantum criticality and development of antiferromagnetic order in the quasikagome Kondo lattice $CeRh_{1-x}Pd_xSn$, Phys. Rev. B **96**, 045139 (2017).

[17] T. Kurumaji, T. Nakajima, M. Hirschberger, A. Kikkawa, Y. Yamasaki, H. Sagayama, H. Nakao, Y. Taguchi, T. Arima, and Y. Tokura, Skyrmion lattice with a giant topological Hall effect in a frustrated triangular lattice magnet, Science **365**, 914 (2019).

[18] H. Wang, Y. Y. Dai, G.-M. Chow, and J. S. Chen, Topological Hall transport: Materials, mechanisms and potential applications, Prog. Mater. Sci. **130**, 100971 (2022).

[19] M. Hirschberger, T. Nakajima, S. Gao, L. C. Peng, A. Kikkawa, T. Kurumaji, M. Kriener, Y. Yamasaki, H. Sagayama, H. Nakao, K. Ohishi, K. Kakurai, Y. Taguchi, X. Z. Yu, T.-h. Arima, and Y. Tokura, Skyrmion phase and competing magnetic orders on a breathing kagome lattice, Nat. Commun. **10**, 5831 (2019).

[20] J. A. Blanco, B. Fåk, E. Ressouche, B. Grenier, M. Rotter, D. Schmitt, J. A. Rodríguez-Velamazán, J. Campo, and P. Lejay, Magnetic field and temperature dependence of the amplitude-modulated magnetic structure of $PrNi_2Si_2$ determined by single-crystal neutron diffraction, Phys. Rev. B **82**, 054414 (2010).

[21] J. Gunasekera, L. Harriger, A. Dahal, A. Maurya, T. Heitmann, S. M. Disseler, A. Thamizhavel, S. Dhar, D. J. Singh, and D. K. Singh, Electronic nature of the lock-in magnetic transition in $CeXAl_4Si_2$, Phys. Rev. B **93**, 155151 (2016).

[22] M. Witt, J. Bönnighausen, F. Eustermann, A. Savourat, J. P. Scheifers, B. P. T. Fokwa, C. Doerenkamp, H. Eckert, and O. Janka, Extending the knowledge on the quaternary rare-earth nickel aluminum germanides of the $RNiAl_4Ge_2$ series ($R =$ Y, Sm, Gd-Tm, Lu)-structural, magnetic and NMR-spectroscopic investigations, Z. Naturforsch. B: J. Chem. Sci. **75**, 149 (2020).

[23] C. C. Zhang, Y. Wang, F. Y. Zhang, H. T. Rong, Y. Q. Cai, L. Wang, X.-M. Ma, S. Guo, Z. J. Chen, Y. N. Wang, Z. C. Jiang, Y. C. Yang, Z. T. Liu, M. Ye, J. H. Lin, J. W. Mei, Z. Y. Hao, Z. J. Xie, and C. Y. Chen, Multiple surface states, nontrivial band topology and antiferromagnetism in $GdAuAl_4Ge_2$, Chin. Phys. B **32**, 077401 (2023).

[24] K. K. Feng, I. A. Leahy, O. Oladehin, K. Wei, M. Lee, and R. Baumbach, Magnetic ordering in $GdAuAl_4Ge_2$ and

$TbAuAl_4Ge_2$: Layered compounds with triangular lanthanide nets, J. Magn. Magn. Mater. **564**, 170006 (2022).

[25] I. A. Leahy, K. K. Feng, R. Dery, R. Baumbach, and M. Lee, Field-induced magnetic states in the metallic rare-earth layered triangular antiferromagnet $TbAuAl_4Ge_2$, Phys. Rev. B **106**, 094426 (2022).

[26] S. Zhang, N. Aryal, K. Huang, K.-W. Chen, Y. Lai, D. Graf, T. Besara, T. Siegrist, E. Manousakis, and R. E. Baumbach, Electronic structure and magnetism in the layered triangular lattice compound $CeAuAl_4Ge_2$, Phys. Rev. Mater. **1**, 044404 (2017).

[27] M. R. Cong, H. Ge, L. Zhang, W. J. Ren, N. Zhao, T. T. Li, S. M. Wang, J. L. Zhu, J. W. Mei, Q. Zhang, J. M. Sheng, F. Gao, B. Li, Z. D. Zhang, and L. S. Wu, Magnetic phase diagram and multiple field-induced states in the intermetallic triangular-lattice antiferromagnet $NdAuAl_4Ge_2$ with Ising-like spins, Phys. Rev. Mater. **7**, 024423 (2023).

[28] S. Shin, P. F. S. Rosa, F. Ronning, J. D. Thompson, B. L. Scott, S. Lee, H. Jang, S.-G. Jung, E. Yun, H. Lee, E. D. Bauer, and T. Park, Synthesis and characterization of the heavy-fermion compound $CePtAl_4Ge_2$, J. Alloys Compd. **738**, 550 (2018).

[29] S. Shin, V. Pomjakushin, L. Keller, P. F. S. Rosa, U. Stuhr, C. Niedermayer, R. Sibille, S. Toth, J. Kim, H. Jang, S.-K. Son, H.-O. Lee, T. Shang, M. Medarde, E. D. Bauer, M. Kenzelmann, and T. Park, Magnetic structure and crystalline electric field effects in the triangular antiferromagnet $CePtAl_4Ge_2$, Phys. Rev. B **101**, 224421 (2020).

[30] V. O. Garlea, B. C. Chakoumakos, S. A. Moore, G. B. Taylor, T. Chae, R. G. Maples, R. A. Riedel, G. W. Lynn, and D. L. Selby, The high-resolution powder diffractometer at the high flux isotope reactor, Appl. Phys. A: Mater. Sci. Process. **99**, 531 (2010).

[31] S. Calder, K. An, R. Boehler, C. R. Dela Cruz, M. D. Frontzek, M. Guthrie, B. Haberl, A. Huq, S. A. J. Kimber, J. Liu, J. J. Molaison, J. Neuefeind, K. Page, A. M. dos Santos, K. M. Taddei, C. Tulk, and M. G. Tucker, A suite-level review of the neutron powder diffraction instruments at Oak Ridge National Laboratory, Rev. Sci. Instrum. **89**, 092701 (2018).

[32] M. Avdeev and J. R. Hester, ECHIDNA: A decade of high-resolution neutron powder diffraction at OPAL, J. Appl. Crystallogr. **51**, 1597 (2018).

[33] C.-M. Wu, G. Deng, J. S. Gardner, P. V orderwisch, W.-H. Li, S. Yano, J.-C. Peng, and E. Imamovicc, SIKA-the multiplexing cold-neutron triple-axis spectrometer at ANSTO, J. Instrum. **11**, P10009 (2016).

[34] S. Yano, G. N. Iles, J.-Ch. Peng, and Ch.-M. Wu, Current status of the taiwanese cold triple axis spectrometers, SIKA, at ANSTO, J. Surf. Invest.: X-Ray, Synchrotron Neutron Tech. **14**, S207 (2020).

[35] A. J. Studer, M. E. Hagen, and T. J. Noakes, Wombat: The high-intensity powder diffractometer at the OPAL reactor, Physica B (Amsterdam, Neth.) **385**, 1013 (2006).

[36] D. Richard, M. Ferrand, and G. J. Kearley, Analysis and visualization of neutron-scattering data, J. Neutron Res. **4**, 33 (1996).

[37] L. B. McCusker, R. B. Von Dreele, D. E. Cox, D. Louër, and P. Scardi, Rietveld refinement guidelines, J. Appl. Crystallogr. **32**, 36 (1999).

[38] J. Rodríguez-Carvajal, Recent advances in magnetic structure determination by neutron diffraction, Physica B (Amsterdam, Neth.) **192**, 55 (1993).

[39] S. V. Gallego, E. S. Tasci, G. de la Flor, J. M. Perez-Mato, and M. I. Aroyo, Magnetic symmetry in the Bilbao Crystallographic Server: A computer program to provide systematic absences of magnetic neutron diffraction, J. Appl. Crystallogr. **45**, 1236 (2012).

[40] J. M. Perez-Mato, S. V. Gallego, E. S. Tasci, L. Elcoro, G. de la Flor, and M. I. Aroyo, Symmetry-based computational tools for magnetic crystallography, Annu. Rev. Mater. Res. **45**, 217 (2015).

[41] See supplemental material at http://link.aps.org/supplemental/10.1103/PhysRevB.109.134407 for temperature-dependent magnetization and electrical resistivity under various applied fields, refined structural parameters, and Rietveld refinement plots of $HoPdAl_4Ge_2$.

[42] J. M. Sheng, L. Wang, A. Candini, W. R. Jiang, L. L. Huang, B. Xi, J. Z. Zhao, H. Ge, N. Zhao, Y. Fu, J. Ren, J. Yang, P. Miao, X. Tong, D. P. Yu, S. M. Wang, Q. H. Liu, M. Kofu, R. Mole, G. Biasiol *et al.*, Two-dimensional quantum universality in the spin-1/2 triangular-lattice quantum antiferromagnet $Na_2BaCo(PO_4)_2$, Proc. Natl. Acad. Sci. USA **119**, e2211193119 (2022).

[43] J. Guo, X. G. Zhao, S. O. Kawamura, L. S. Ling, J. F. Wang, L. H. He, K. Nakajima, B. Li, and Z. D. Zhang, Magnetic-field and composition tuned antiferromagnetic instability in the quantum spin-liquid candidate $NaYbO_2$, Phys. Rev. Mater. **4**, 064410 (2020).

[44] D. Gignoux and D. Schmitt, Commensurability versus incommensurability in rare-earth intermetallic compounds, J. Magn. Magn. Mater. **129**, 53 (1994).

[45] M. Amara, Dynamical splitting of cubic crystal field levels in rare-earth compounds, Phys. Rev. B **99**, 174405 (2019).

[46] V. K. Anand, D. T. Adroja, A. Bhattacharyya, A. D. Hillier, J. W. Taylor, and A. M. Strydom, Investigations of the singlet ground state system: $PrIrSi_3$, J. Phys.: Condens. Matter **26**, 306001 (2014).

[47] F. Gao, H.-L. Wang, M. Y. Cui, W. J. Ren, C.-W. Wang, S. Yano, X. Z. Liu, Z. Z. He, B. Li, and Z. D. Zhang, Noncollinear commensurate antiferromagnetic structure in metallic $Pr_2PdAl_7Ge_4$, Phys. Rev. B **107**, 214435 (2023).

[48] J. W. Lynn, S. Skanthakumar, Q. Huang, S. K. Sinha, Z. Hossain, L. C. Gupta, R. Nagarajan, and C. Godart, Magnetic order and crystal structure in the superconducting RNi_2B_2C materials, Phys. Rev. B **55**, 6584 (1997).

[49] M. Reehuis, B. Fehrmann, M. W. Wolff, W. Jeitschko, and M. Hofmann, Antiferromagnetic order in $TbFe_2Al_10$ and $DyFe_2Al_10$, Physica B (Amsterdam, Neth.) **276**, 594 (2000).

[50] M. Reehuis, M. W. Wolff, A. Krimmel, E.-W. Scheidt, N. Stüsser, A. Loidl, and W. Jeitschko, Magnetic phase transitions in $TbFe_2Al_{10}$, $HoFe_2Al_{10}$, and $ErFe_2Al_{10}$, J. Phys.: Condens. Matter **15**, 1773 (2003).

[51] J. Robert, F. Damay, K. Saito, A. M. Bataille, F. Porcher, G. André, A. Gukasov, J.-M. Mignot, H. Tanida, and M. Sera, Neutron diffraction study of magnetic order in $NdFe_2Al_{10}$, Phys. Rev. B **90**, 224425 (2014).

[52] D. Gignoux, J. C. Gomez-Sal, R. Lemaire, and A. de Combarieu, Specific heat and modulated magnetic structures in the $HoNi_{0.5}Cu_{0.5}$ and $ErNi_{0.6}Cu_{0.4}$ compounds, Solid State Commun. **21**, 637 (1977).

[53] R. White, W. D. Hutchison, T. Mizushima, and A. J. Studer, Evolution of the magnetic structure of $TbRu_2Al_{10}$ in applied field, J. Alloys Compd. **679**, 169 (2016).

[54] H. Kageyama, Y. Narumi, K. Kindo, K. Onizuka, Y. Ueda, T. Goto, Quantized magnetization plateau in the orthogonal dimer system $SrCu_2(BO_3)_2$, J. Alloys Compd. **317**, 177 (2001).

[55] D. Gignoux and D. Schmitt, Competition between commensurate and incommensurate phases in rare-earth systems: Effects on H-T magnetic phase diagrams, Phys. Rev. B **48**, 12682 (1993).

[56] H. Nojiri, M. Uchi, S. Watamura, M. Motokawa, H. Kawai, Y. Endoh, and T. Shigeoka, Neutron diffraction study of $PrCo_2Si_2$ in pulsed high magnetic field, J. Phys. Soc. Jpn. **60**, 2380 (1991).

[57] J. A. Blanco, D. Gignoux, D. Schmitt, and C. Vettier, Field induced magnetic structures in $TbNi_2Si_2$, J. Magn. Magn. Mater. **97**, 4 (1991).

[58] A. R. Ball, D. Gignoux, D. Schmitt, F. Y. Zhang, and M. Reehuis, Field induced magnetic structures in hexagonal HoAlGa, J. Magn. Magn. Mater. **110**, 343 (1992).

[59] A. Hiess, F. Bourdarot, P. Burlet, E. Ressouche, J.-P. Sanchez, F. Wastin, J. Rebizant, G. H. Lander, and E. Suard, Magnetic structure of $NpPd_2Al_3$: Relevance to the coexistence of superconductivity and magnetism in UPd_2Al_3, Phys. Rev. B **55**, 1138 (1997).